Weierstraß-Institut
für Angewandte Analysis und Stochastik
Leibniz-Institut im Forschungsverbund Berlin e. V.

Beam combining scheme for high-power broad-area semiconductor lasers with Lyot-filtered reinjection: Modeling, simulations, and experiments

Carsten Brée[1], Volker Raab[2], Joan Montiel-Ponsoda[3], Guillermo Garre-Werner[3],

Kestutis Staliunas[4], Uwe Bandelow[1], Mindaugas Radziunas[1]

submitted: April 9, 2019

[1] Weierstrass Institute
Mohrenstr. 39
10117 Berlin
Germany
E-Mail: carsten.bree@wias-berlin.de
        uwe.bandelow@wias-berlin.de
        mindaugas.radziunas@wias-berlin.de
	[2] Raab-Photonik GmbH
	Amundsenstr. 10
	14469 Potsdam
	Germany
	E-Mail: raab@optikexpertisen.de

[3] Monocrom S.L. Carrer de la Vilanoveta 6 08800 Vilanova i la Geltrú Spain E-Mail: j.montiel@monocrom.com g.garre@monocrom.com	[4] Departament de Física i Enginyeria Nuclear Universitat Politècnica de Catalunya Colom 11 08222 Terrassa Spain E-Mail: kestutis.staliunas@icrea.cat

No. 2586

Berlin 2019

Beam combining scheme for high-power broad-area semiconductor lasers with Lyot-filtered reinjection: Modeling, simulations, and experiments

Carsten Brée, Volker Raab, Joan Montiel-Ponsoda, Guillermo Garre-Werner, Kestutis Staliunas, Uwe Bandelow, Mindaugas Radziunas

Abstract

A brightness- and power-scalable polarization beam combining scheme for high-power, broad-area semiconductor laser diodes is investigated numerically and experimentally. To achieve the beam combining, we employ Lyot-filtered optical reinjection from an external cavity, which forces lasing of the individual diodes on interleaved frequency combs with overlapping envelopes and enables a high optical coupling efficiency. Unlike conventional spectral beam combining schemes with diffraction gratings, the optical coupling efficiency is insensitive to thermal drifts of laser wavelengths. This scheme can be used for efficient coupling of a large number of laser diodes and paves the way towards using broad-area laser diode arrays for cost-efficient material processing, which requires high-brilliance emission and optical powers in the kW-regime.

1 Introduction

High-power broad-area edge-emitting semiconductor lasers (BALs) are key devices in many modern applications, like remote sensing, pumping of solid-state, fiber, and gas lasers, medical applications, and material processing. In recent years, the optical output power of modern, high-power broad-area semiconductor laser has increased to some thirty Watts [1]. By using laser diode arrays and suitable beam combining techniques, this makes BALs highly relevant for cost-efficient material processing, which requires high-brilliance emission and optical power in the kW-regime. While side-by-side beam combining schemes are power scalable, these schemes lack scalability of beam brightness, since the combined, beam parameter product (BPP) scales linearly with the number of laser diodes. This drawback can be circumvented by exploiting different spectral beam combining schemes where the array elements, operating at different narrow, non-overlapping wavelength windows, are collected into the single beam utilizing various diffractive optical elements, see, e.g., Ref. [2]. The near and far fields of individual emitters, in this case, can be overlapped, such that BPP of the combined beam is more or less preserved, whereas intensity and, thus, brightness is scaled with the number of coupled emitters. There are several disadvantages to this scheme, however. On the one hand, this is an increased width of the optical spectra of this combined beam, such that a combination of a large number of emitters requires a sufficiently broad gain spectrum. On the other hand, the optical coupling efficiency of such a beam combining scheme is highly sensitive to thermal drifts of the central wavelength of the individual lasers. The problems related to the spectral broadening and thermal shifts can be solved when applying polarization beam combining. In this case, two orthogonally polarized laser beams are spatially superimposed using a polarizing beam splitter. However, the latter scheme, in general, produces unpolarized output radiation and can be used for a combination of only two emitters.

In this paper, we analyze a polarization and spectral beam combining technique which can be employed for coupling BALs with a similar emission wavelength and is insensitive to thermal drifts of the individual frequencies. Moreover, our demonstrated scheme is cascadable, as it produces a combined output beam with a well-defined polarization state [3]. Our beam combining scheme of the emitters is based on a common external cavity (EC) which contains a Lyot filter and provides an individually filtered optical reinjection to each emitter. As will be shown, the spectrally filtered reinjection leads to a self-adjustment of the spectral output of the BALs to interleaved frequency combs with overlapping envelopes, which enables a high optical coupling efficiency.

Our theoretical analysis is based on numerical simulations of the compound BAL+EC system, where dynamics of BALs is governed by the 2 (space) + 1 (time) - dimensional traveling wave (TW) model [4], whereas field propagation within the EC and its reinjection into the BALs are defined by an efficient model derived below in this work. Up to our knowledge, modeling and simulation of such BAL+EC configuration are made for the first time in this paper.

Our paper is arranged as follows. In Section 2, the simplest setup of two polarization-coupled emitters is presented and discussed. Section 3 is devoted to a short description of the dynamical model of high-power BALs and the corresponding solver as well as to the derivation of the efficient model of Lyot-filtered optical reinjection to the emitters. The set of simulations presented in Section 4 demonstrates the selection of the lasing wavelengths by filtered optical feedback and discusses the dependence of beam combining efficiency on several parameters of the EC. Whereas Section 5 gives experimental evidence of the beam combining, Section 6 discusses further possible extensions of the considered beam combining scheme. Finally, in Appendix, we have collected technical details of the reinjection model.

2 Setup

An introduction of fast- and slow-axis collimating lenses, polarization-rotating half-wave plates (HWPs), polarizing beamsplitters (PBSs), and birefringent crystals (BCs) into the EC allows construction of the coupled laser-EC system containing several BALs with interleaved frequency combs of the optical spectra. The emission of individual BALs can be efficiently combined into a single beam of the same polarization. Whereas the number of coupled BALs should scale the intensity of the combined beam, the width of the combined optical spectra, near- and far- fields should be comparable to those of the individual emitters.

The laser setup discussed in this work is schematically represented in Fig. 1 and was originally introduced in [3]. Here we analyze coupling of two BALs, BAL$_1$ and BAL$_2$, each emitting horizontally polarized component E_x of the vector field $\mathbf{E} = \begin{pmatrix} E_x \\ E_y \end{pmatrix}$, what is indicated by symbol $\updownarrow$ in Fig. 1. Directly at the front facets of both BALs, there are two fast-axis collimating (FAC) lenses (not indicated in the scheme), which are assumed to provide perfect collimation of the beam spreading along the fast (y-) axis. Another pair of slow-axis-collimating (SAC) lenses of focal distance f are located perpendicularly to the optical axes of both BALs at the (optical) distance f from their front facets. To swap between the horizontally and vertically polarized field components, the (zero order) HWP is located just after the SAC lens attributed to BAL$_2$. Consequently, the field emitted by the BAL$_2$ after this HWP has only E_y component, as indicated by the symbol $\odot$ in the same figure. To realize spectral filtering of the emission, the EC contains a Lyot-filtering element consisting of PBS$_1$, PBS$_2$, and a (calcite) BC of specially selected length L in between. Orientation and location of PBS$_1$ w.r.t. optical axes of both BALs is such that it permits the transmission of the E_x-component from BAL$_1$ and of E_y-component

from the BAL$_2$ branch towards EC mirror. The optic axis of the BC is under $45°$ to the lateral (x) and vertical (y) directions. To avoid parasitic backreflections, all optical elements have antireflective (AR) coatings.

During its transmission through the BC, the combined two-component vector field undergoes a wavelength-dependent change of polarization state. By its length L and birefringence coefficient, the BC prescribes two discrete periodic sets of wavelengths λ_s, λ_c with λ_c shifted by a half-period w.r.t. λ_s. While the BC maintains the polarization state for incident wavelengths around λ_s, vectorial components E_x, E_y are swapped for incident radiation at wavelengths around λ_c. The subsequent PBS$_2$ transmits only the E_x-component of the BC-transmitted radiation. Hence, from the x-polarized BAL$_1$ emission, the Lyot filter eliminates (i.e., distributes to a beam dump) λ_c spectral components, while it eliminates λ_s spectral components of the BAL$_2$ emission, which is rotated to y-polarization by the HWP before passing the Lyot filter. At the semitransparent outcoupling mirror, a dominant fraction of the x-polarized radiation is transmitted, while a smaller part is reflected towards the Lyot filter. With the same reasoning as above, one concludes that PBS$_1$ distributes back-reflected spectral content around λ_s towards BAL$_1$, while spectral components around λ_c are reinjected into BAL$_2$.
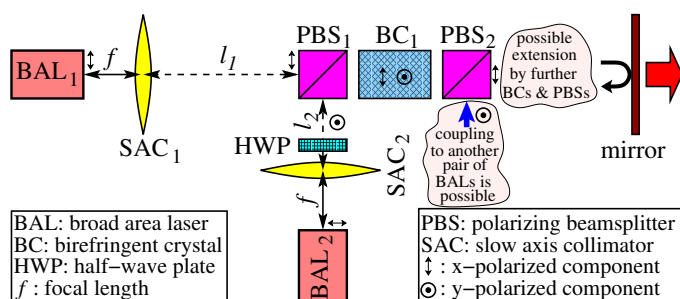

Figure 1: Schematic representation of a pair of polarization-coupled BALs with an indication of possible extensions of this scheme by another pair of the emitters and/or additional BCs and PBSs.

In our previous theoretical study of a single BAL with filtered reinjection [5], we have shown that even though the presence of the Lyot filter within the EC implies a suppression of the emission at certain periodically repeated wavelengths, the overall emission intensity remains only weekly affected by the filter. That is, the missing lasing at certain wavelength bands is compensated by a larger contribution of the remaining wavelength components. This intensity preservation we intend to exploit in the polarization coupling scheme discussed in this paper. In the ideal case of the perfect wavelength selection by the filtered feedback, both BAL$_1$ and BAL$_2$ emit only at the fixed periodically interchanging wavelengths λ_s and λ_c, respectively. For the combined beam, we expect preservation of the spectral, near-field, and far-field widths as well as nearly doubling of the solitary BAL intensity in this case. The main optical losses within the considered EC occur at PBS$_2$, where part or even whole spectral components of BAL$_1$ (BAL$_2$) located outside of λ_s (λ_c) have y-polarization and are neither redirected to the external mirror nor reinjected into the BALs. It is noteworthy, that the presented configuration of two coupled BALs, in general, can be cascaded, extending it by additional waveplates, PBSs, BC, and another two and even more emitters. This possibility will be briefly discussed in Section 6.

3 Model

3.1 Dynamical model of broad-area laser

Our model of BAL is based on the decomposition of the dominant fundamental transverse electric component of the electromagnetic wave into two along the longitudinal axis (z-coordinate) counter-

propagating fields,

$$\mathcal{E}(\mathbf{r}, t) = \Phi(y)(E^+(z, x, t) + E^-(z, x, t))e^{i\omega_0 t} + c.c.,$$

where $E^\pm(z, x, t) = u^\pm(z, x, t)e^{\mp i\bar{n}k_0 z}$, $\Phi(y)$ is the vertical mode profile, $\bar{n}$ is the refractive index of the material, $k_0 = 2\pi/\lambda_0$ is the free-space central wavenumber (λ_0: central wavelength), and $\omega_0 = k_0 c_0$ is the constant optical reference frequency (c_0: speed of light in vacuum). By substituting this decomposition into Maxwell's equations and applying the slow-varying envelope approximation one can derive the following 2 (space) + 1 (time) - dimensional traveling wave (TW) equations for the spatiotemporal evolution of the slowly varying complex amplitudes $u^+(z, x, t)$ and $u^-(z, x, t)$:

$$\frac{\tilde{n}_s}{c_0}\partial_t u^\pm = \left[\mp\partial_z - \frac{i}{2k_0\bar{n}_s}\partial_{xx} - i\beta\right]u^\pm + F_{sp}^\pm. \tag{1}$$

Here $\tilde{n}_s$, $\bar{n}_s$, and $F_{sp}^\pm$ are the group velocity and the reference refractive indices in semiconductor, and the Langevin noise term, respectively. The complex propagation factor $\beta(z, x, t)$ in (1) accounts for linear and nonlinear (two-photon) absorption [6], the built-in and the dynamic contributions to the excess refractive index, and the material gain. The last two factors depend on the excess carrier density and take into account nonlinear gain compression [6] and material gain dispersion. To mimic a heating-induced red-shift of the lasing wavelengths and a corresponding broadening of the far-fields, we assume additional linear bias current I-dependent contributions to the gain peak wavelength and the excess refractive index, $\delta_{\bar{n}}^h = (c_{\bar{n}}^h + L_{\bar{n}}^h(x))I$ [4]. The heating-induced lateral profile $L_{\bar{n}}^h(x)$ within the emitter can be approximated by a negative parabola [7] or, even better, by a suitable Lorentzian or supergaussian, but, in general, should be estimated experimentally or precomputed using the heat transport model defined within the transversal cross-section of the BAL [8]. The amplitude of $L_{\bar{n}}^t$ in our case was about 10^{-4} A^{-1}. A diffusive rate equation governs the dynamics of the carrier densities. Finally, to close the TW model, we apply the boundary conditions

$$u^+(-l, x, t) = \sqrt{R_{-l}}u^-(-l, x, t), \quad u^-(0, x, t) = \sqrt{R_0}u^+(0, x, t) + (1 - R_0)[\mathcal{F}u^+](x, t), \tag{2}$$

where parameters R_{-l} and R_0 are the intensity reflection coefficients at the (high-reflective) rear and (low-reflective) front facets $z = -l$ and $z = 0$, respectively, of the diode (l: the length of the BAL), whereas $\mathcal{F}$ is a linear operator determining optical feedback. Assuming that the beam collimation along the fast axis (y direction) is perfect, optical feedback $[\mathcal{F}u^+]$ in (2) can be written as a general linear integral operator,

$$[\mathcal{F}u^+] = \int_{-\infty}^t \int_{\mathbb{R}} K(x', x, t', t)u^+(0, x', t')dx'dt', \tag{3}$$

where the kernel function $K(x', x, t', t)$ depends on the configuration of the EC.

For numerical integration of the TW model, we exploit the software kit `BALaser` [9] developed at the Weierstrass Institute in Berlin. The numerical algorithm is based on the split-step fast-Fourier-transform (FFT) based method for the field equations (1) and finite difference approximations for the carrier rate equations. The numerical resolution of optical fields and carrier density at fixed z and t requires $\mathcal{O}(N_x \log(N_x))$ arithmetic operations (N_x: number of equidistant lateral points used for numerical discretization of dynamical variables). For the acceleration of time-consuming calculations, the numerical algorithm was parallelized using distributed-memory paradigm and executed on multicore compute servers. As a consequence, instead of ~ 2 hours required for simulation of 1-ns long transients of a typical BAL using the single process on a single core of our server, we perform the same simulations with 30 processes in about 5 minutes. For more details on the algorithms used to solve the TW model see Refs. [4, 10]. In our work, we have simulated $l = 4$ mm long BALs having $100\,\mu$m
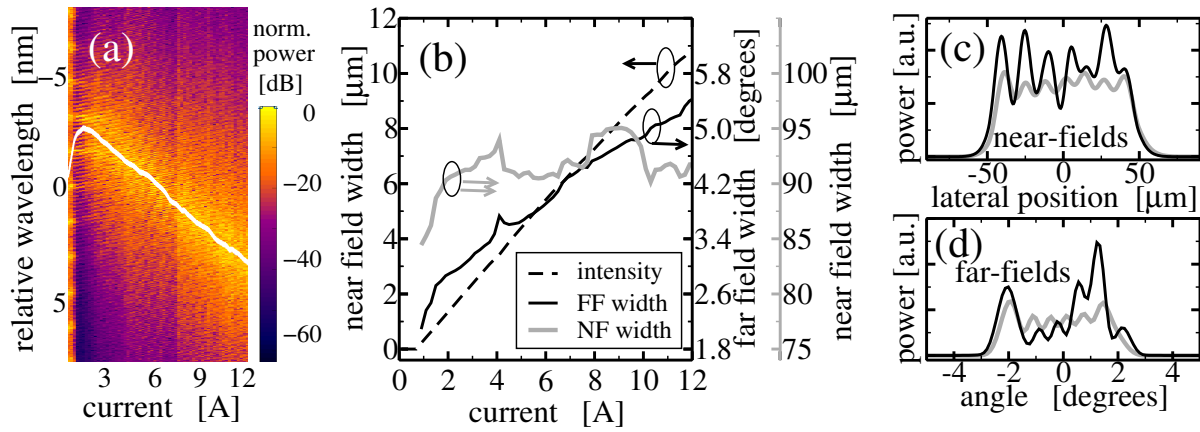
Figure 2: Simulations of the solitary BAL. Mapping of the optical spectra with an indication of the mean wavelength (a), mean emission intensity (dashed) and width (95 % of the power content) of the far (black solid) and near (grey solid) fields (b) as functions of the emitter current I, near (c) and far (d) fields for $I = 8$ A (grey) and $I = 10$ A (black).

width of the contact stripe, and operating at about $\lambda_0 = 975$ nm wavelength. Other parameters were $\bar{n}_s = 3.42$, $\tilde{n}_s = 3.915$, $R_{-l} = 0.95$, $R_0 = 0.04$, whereas the parameters defining gain dispersion, propagation factor β, and carrier rate equations are similar to those used in Refs. [4, 6]. For $\mathcal{F} = 0$, the model above allows simulating the dynamics in solitary BA laser. Fig. 2 presents an extensive study of such a laser for tuned bias current parameter I. A pair of such lasers coupled through the common EC will be used in the following numerical examples of this paper.

3.2 Model of the optical feedback

In the case of m BALs sharing the same EC ($m = 2$ in the present case) we need to solve m sets of the TW models (1), (2) for the functions $u_j^\pm$, $j = 1, \ldots, m$, supported by the corresponding set of carrier rate equations. The optical feedback term $[\mathcal{F}u^+]_r$ for each laser should account for the fields emitted by all BALs:

$$[\mathcal{F}u^+]_r(x,t) = \sum_{j=1}^{m} M_{[r,j]} u_j^+(0, x, t), \tag{4}$$

where operators $M_{[r,j]}$ represent the field propagation from the BAL$_j$ to the BAL$_r$ and, in general, are integral operators of the type (3). The major challenge is the derivation of the models for the propagators $M_{[r,j]}$ and efficient implementation of these models into our solver. By "efficient" we mean an implementation requiring not more than $\mathcal{O}(N_x \log(N_x))$ arithmetic operations for evaluation of the function $[\mathcal{F}u^+]_r(x,t)$ at each time moment t. This is a crucial requirement seeking to avoid a significant slow-down of our simulations.

For this reason, when modeling the beam propagation within the EC, we neglect the angular dependencies of optical path lengths, i.e., assume that the beam propagation time $d\tilde{n}/c_0$ through the homogeneous material is independent on the lateral position and is fully determined by the length d and the group index $\tilde{n}$ of this material. We consider field propagation in a homogeneous material with refractive index $\bar{n}$ in the paraxial regime, i.e., we assume small incident angles $|k_x/k_0| \ll 1$. Then, the angular dispersion relation for forward waves, $k_z = \sqrt{\bar{n}^2 k_0^2 - k_x^2}$, can be approximated by the parabolic dispersion relation $k_z \approx \bar{n}k_0 - \frac{k_x^2}{2\bar{n}k_0}$, which leads to Huygens-Fresnel diffraction integrals w.r.t. the slow-axis coordinate x. Together with the perfect fast-axis collimation, these assumptions

for each optical element or homogeneous material give rise to a set of scalar operators M relating incident and outgoing fields, $E^i(x,t)$ and $E^o(x,t) = ME^i(x,t)$, as well as (2×2)-dimensional matrix operators $\mathbf{M}$ acting on the vector-field $\mathbf{E} = \begin{pmatrix} E_x \\ E_y \end{pmatrix}$ containing horizontally and vertically polarized components E_x and E_y. These matrix-operators are relevant when modeling the field transmission through PBSs, HWPs, and, especially, BC with a crystal optical axis rotated by $45°$ against the x-axis. In the last case, we use unitary (2×2)-dimensional Jones matrix operators accounting for angular dispersion and phase retardation between the ordinary and extraordinary beam components [11]. The propagation of these components along the BC is determined by different sets of refractive and group indices, $(\bar{n}_1, \tilde{n}_1)$ for ordinary axis and $(\bar{n}_2, \tilde{n}_2)$ for extraordinary one. The definitions of all relevant propagators through different optical components are collected in Appendix.

The subsequent application of the corresponding "elementary" operators to the x-polarized front-facet emission $\mathbf{E}_j(x,t) = (u_j^+(0,x,t),\, 0)^T$ of each BAL enables us finding the total combined field $\mathbf{E}^t$ just after the external mirror as well as the optical feedback $\mathbf{E}_r^f$ to each BAL:

$$\mathbf{E}^t = \sqrt{1 - R_e} \sum_j \mathbf{M}_{[j]} \mathbf{E}_j, \quad \mathbf{E}_r^f = \sum_j \mathbf{M}_{[r,j]} \mathbf{E}_j, \quad \mathbf{M}_{[r,j]} = \sqrt{R_e}\, \mathbf{M}_{[r]}^T \mathbf{M}_{[j]}. \tag{5}$$

Here $\mathbf{M}_{[j]}$ is the optical field propagator from the front facet of BAL$_j$ to the external mirror, ^{T} denotes the matrix transposition, whereas R_e is intensity reflection at the mirror. The estimation of the feedback and the combined emitted field at each new time iteration requires the consequent application of several "elementary" operators in, probably, laterally extended domain. Since computationally most involved scalar operator, which is a free-space beam propagator M_d^{pr} (see Appendix), requires an application of the FFT algorithm in the lateral space, the straightforward estimation of these fields can be performed with the initially allowed $\mathcal{O}(N_x \log(N_x))$ arithmetic operations.

The commutation properties of different "elementary" operators along with the special configuration of the considered EC admit a significant simplification of the field feedback estimation. On the one hand, since the front facets of the BALs are on the focal planes of the collimating lenses, the whole EC can be interpreted as a linear combination of several optical telescopes with the nonvanishing offset δ between the inner focal planes. The corresponding numerically-inexpensive propagators are defined by the simple lateral-coordinate dependent phase shift, the time shift, and the lateral coordinate swap. On the other hand, we note that only x-polarized component of the vector-fields $\mathbf{E}$ emitted by the BALs can propagate along the whole EC, and the reinjection to the BALs has only x-polarized component. For this reason, all but the upper-left component of each matrix operator $\mathbf{M}_{[r,j]}$ from (5) are vanishing, whereas the nonvanishing scalar component $M_{[r,j]}$ used in (4) is determined by

$$M_{[r,j]} = \frac{\sqrt{R_e}}{4} \sum_{l=1}^3 \xi_{r,j}^l e^{i\frac{k_0}{2f^2}\delta_{r,j}^l x^2} M^{\mathrm{sw}} M_{\tau_{r,j}^l}^{\mathrm{sh}}, \tag{6}$$

where M_τ^{sh}, M^{sw} are time-shift and coordinate swap operators, respectively: $M_\tau^{\mathrm{sh}} A(t) = A(t - \tau)$, $M^{\mathrm{sw}} A(x) = A(-x)$. The parameters $\xi_{r,j}^l$, $\delta_{r,j}^l$, and $\tau_{r,j}^l$ provide the coordinate-independent phase shift, represent the optical pathlength of the offset between the inner focal planes within the corresponding telescope, and are the time needed by the optical field to pass the EC through this telescope, respectively. All these parameters depend on $\bar{n}_j$ and $\tilde{n}_j$, $j = 1, 2$, the length of the BC L, the focal length of the SAC lenses f, the cumulative widths of the air gaps between the corresponding lens and the external mirror l_1 and l_2, the HWP- and lens-induced fixed phase shift factors φ_{wp} and φ_{ln} (see Appendix). The exact definitions of these parameters are collected in (8) in Appendix. In our numerical examples, we have used the following parameters of the EC: $R_e = 0.04$, $f = 20\,\mathrm{mm}$, $L \in [4, 20]\,\mathrm{mm}$, $l_1 = l_2 = 200\,\mathrm{mm} - f - L$ (distance between diode facets and outcoupling mirror fixed at $200\,\mathrm{mm}$, neglected longitudinal extension of the PBS), $\bar{n}_1 = 1.644$, $\bar{n}_2 = 1.480$, $\tilde{n}_1 = 1.666$, $\tilde{n}_2 = 1.487$.

We note that the feedback operator defined in Eqs. (4) and (6) is a digital finite impulse response filter performing time-domain spectral filtering in $\mathcal{O}(m^2 N_x N_\tau)$ operations, where N_τ is the number of different time delays $\tau_{r,j}^l$. This allows an inexpensive implementation of the above-discussed frequency filtered optical feedback scheme into our dynamical solver of BALs.

To get a better idea about frequency (wavelength) filtering properties of the EC, we consider the action of $M_{[r,j]}$ on the frequency-domain Fourier components $\hat{E}_j^i(x, \omega')e^{i\omega't}$ of the fields $E_j^i(x, t)$, $j = 1, 2$, (ω': a detuning from the central frequency ω_0). The corresponding response functions can be written in the matrix format,

$$\begin{pmatrix} \hat{E}_1^o \\ \hat{E}_2^o \end{pmatrix} = \sqrt{R_e}\, \xi' M^{\mathrm{sw}} \begin{pmatrix} \hat{\xi}_{1,1} \cos^2 \frac{\gamma'}{2} & \frac{\hat{\xi}_{1,2}}{2} \sin \gamma' \\ \frac{\hat{\xi}_{2,1}}{2} \sin \gamma' & \hat{\xi}_{2,2} \sin^2 \frac{\gamma'}{2} \end{pmatrix} \begin{pmatrix} \hat{E}_1^i \\ \hat{E}_2^i \end{pmatrix},$$

$$\text{where} \qquad \gamma' = -Lk_0\Big(\Delta_{\bar{n}}(1 + \tfrac{x^2}{2\bar{n}_1\bar{n}_2 f^2}) + \tfrac{\Delta_{\tilde{n}}\omega'}{c_0 k_0}\Big),$$

(7)

$\Delta_{\bar{n}} = \bar{n}_1 - \bar{n}_2$, $\Delta_{\tilde{n}} = \tilde{n}_1 - \tilde{n}_2$, while ξ' and $\hat{\xi}_{r,j}$, which are unique and individual for all $M_{[r,j]}$ phase shifts, are defined in (9) in Appendix. γ' implies changes in the amplitude of the response functions with changing frequency ω' and coordinate x. The periodic dependence of the filtering amplitude on the optical frequency detuning ω' (or on the relative wavelength $\lambda \approx -\frac{\lambda_0^2}{2\pi c_0}\omega'$) is a dominant effect deciding filtering characteristics of the EC, see Fig. 3 where reflection and transmission spectra induced by the BC with $L = 4\,\mathrm{mm}$ are collected. We admit here, that a small overlapping of both self-reflection spectra and a moderate cross-feedback spectra, see Fig. 3(a), do not exclude coexistence of the common wavelength contributions in both BALs which can be disturbing when seeking the optimal combining of two beams. A possible improvement of the EC-induced filtering properties will be shortly addressed in Section 6. The dependence of the EC filtering on the lateral position will be considered in the following section.
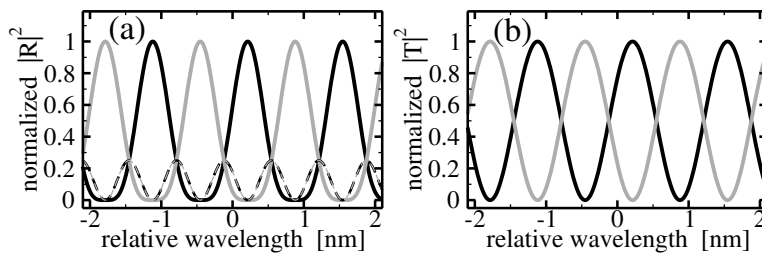

Figure 3: Normalized reflection (a) and transmission (b) spectra of the EC from Fig. 1. Black and grey: filtering of the fields emitted by BAL$_1$ and BAL$_2$, respectively. Thick solid and thin dashed in (a): self- and cross- feedback.

4   Simulations

Direct numerical simulations were carried out for different injection currents, calcite crystal lengths, SAC focal lengths, and external mirror reflectivities. Time- and spatially dependent, complex optical near fields were recorded for $4\,\mathrm{ns}$, after an initial transient of $16\,\mathrm{ns}$, both at the diode output facets, and after transmission through the EC. All depicted optical spectra were obtained by taking the lateral average of the intensities of the temporal Fourier transform of the recorded complex fields.

To calculate the EC transmitted optical fields, a second lens of same focal length as the SAC is placed at a focal distance behind the EC mirror, and optical fields are recorded at the rear focal plane of the second lens. This allows to use the same formalism derived for calculating the optical feedback (Subsection 3.2) but with a single transmission through the Lyot filter element and halved free-space

optical path lengths, i.e., $l_l \rightarrow l_l/2$. To estimate the efficiency of our beam combining scheme, we introduce a coupling efficiency $\eta = P/\sum_{l=1}^{m} P_l$, where P is the optical power contained in the EC transmitted, combined beam, and P_j are optical powers calculated at the front facets of BAL_j, $j = 1, \ldots, m$, respectively ($m = 2$ in the discussion below). In the ideal case, the efficiency η can be close to 1. A further, decisive factor for evaluating the quality of our beam combing scheme is the (slow-axis) beam parameter product factor $BPP_{sl} = D_0\Theta_0/4$, where Θ_0 and D_0 are beam divergence and beam waist at 95% power content, respectively. To determine Θ_0, we calculate the time-dependent far-fields $\bar{E}(\theta, t)$ ($\sim$ Fourier transformed complex near fields $E(x, t)$) and estimate the width of their time-averaged intensities, $\langle|\bar{E}(\theta, t)|^2\rangle_t$. To find $D_0 = \min_d D(d)$, we estimate the widths $D(d)$ of the time-averaged intensities of the free-space propagated fields, $\langle|M_d^{\text{pr}}E(x, t)|^2\rangle_t$, for a series of distances d.

In Fig. 4, simulation results are shown for calcite crystal length of $L = 4$,8, and 12 mm and an SAC focal length $f = 20$ mm. Both diodes were driven at maximum operating current $I = 12.6$ A. Shown are optical spectra at the front facets of the individual diodes, and far-field profiles of the combined beam and those at the front facets of both diodes. For all crystal lengths, the individual diodes are lasing on mutually interleaved frequency combs, with comb spacing $\Delta = \frac{2\pi c_0}{L\Delta_{\tilde{n}}}$ (corresponding to the wavelength spacing $\Delta_\lambda \approx \frac{\lambda_0^2}{L\Delta_{\tilde{n}}}$, see left panels of Fig. 4), determined by the crystal length L and the group birefringence $\Delta_{\tilde{n}}$. As the individual combs have little overlap, the simulations show high optical coupling efficiencies of $\eta = 0.87, 0.88, 0.89$ for $L = 4, 8$, and 12 mm. However, our scheme is not completely lossless. Indeed, the spectra reveal that a small fraction of radiation is still excited outside of the Lyot-filter transmission windows of BAL_1 and BAL_2, and, even more, within these windows but outside of the corresponding optimal central transmission wavelengths λ_s or λ_c.
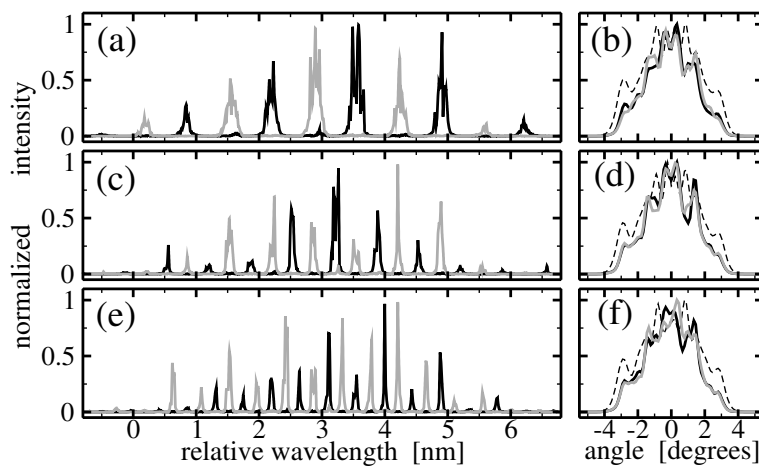

Figure 4: Dependence of the BAL emission on the length L of the BC within the EC. (a) and (b): $L = 4$ mm. (c) and (d): $L = 8$ mm. (e) and (f): $L = 12$ mm. In all cases $f = 2$ cm and $R_e = 0.04$. Left and right panels: optical spectra and angular representations of the emissions. Solid black and grey: emission at the front facet of BAL_1 and BAL_2, respectively. Thin dashed: combined beam after the external mirror.

Far-fields of the individual diodes and combined-beam far fields are shown in the right panels of Fig. 4. The combined beam far-field appears slightly broadened compared to those of the individual diodes, which is due to the large central offset between inner focal planes of the SAC and the additional lens placed behind the EC mirror. However, the calculated slow-axis BPP factors show that our beam combining scheme nearly preserves the beam quality of the individual diodes. In fact, we found beam quality factors of $BPP_{sl} = \{2.28, 2.33, 2.44\}$ (i.e., $\{\text{BAL}_1, \text{BAL}_2, \text{combined beam}\}$) for $L = 4$ mm, $BPP_{sl} = \{2.33, 2.33, 2.46\}$ for $L = 8$ mm, and $BPP_{sl} = \{2.29, 2.3, 2.41\}$ for $L = 12$ mm.

Next, we tuned the BIAS current of the coupled BALs, with simulation results depicted in Fig. 5. The calcite crystal length was $L = 4$ mm, and SAC focal length, as above $f = 20$ mm. In our simulations, we took into account the red-shift of central optical wavelength with injection current due to thermal
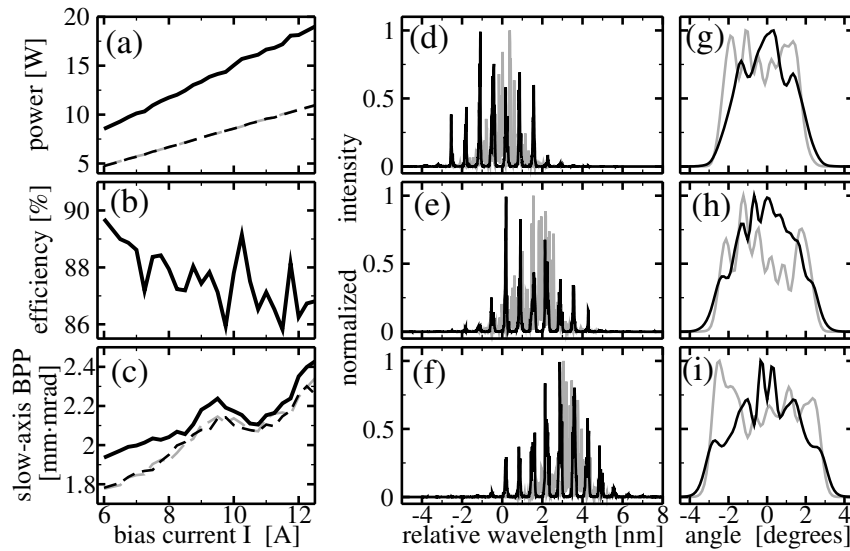
Figure 5: Power of the combined beam and the separate emissions (a), beam coupling efficiency (b), and slow-axis BPP factors of the beams (c) as functions of bias current applied at each of two emitters. Black solid: combined beam after the external mirror. Black and grey thin dashed: emission of BAL_1 and BAL_2 at corresponding front facet. (d), (g): optical spectra and angular representations of the combined beam after the external mirror (black) and of the solitary BAL without optical feedback (grey) for $I = 6$ A, that is applied to each emitter. (e), (h): same for $I = 9$ A. (f), (i): same for $I = 12$ A.

heating. In panel (a) of this figure, optical power versus bias current is shown for the combined beam and for the power emitted by the individual diodes. Interestingly, the combined beam power curve exhibits undulatory behavior, with intermediate plateaus, which are absent in the power curve of the solitary BAL. In panel (b), we show the corresponding coupling efficiency vs. injection current, which has a comparable, oscillating behavior with a strong dependence on injection current. Finally, beam quality factors for the combined beam and the individual beams emitted by both diodes are shown in panel (c). For operating currents above 8 A, the combined beam quality decreases by less than 8% compared to the slow-axis BPP factors of the individual diodes.

The undulatory behavior of the power vs. bias current curve shown in panel (a) may potentially be explained by the gain distribution of the longitudinal BAL modes: with increasing current and heating, the gain spectrum of the BALs is red-shifted relative to the fixed, current-independent transmission windows of the Lyot filter. In consequence, larger combined beam power is expected when the wavelengths of a sufficient number of dominant (i.e., large gain) compound cavity modes coincide with transmission maxima λ_s or λ_c of the Lyot filter. Optical spectra and far-fields of the combined beam and corresponding solitary BAL, are shown in Figs. 5(d)-(i), for the cases of $I = 6, 9$, and 12 A. Indeed, while the position of the spectral envelope is subject to the discussed thermal red-shift, the comb spectral peaks appear at fixed wavelengths, independent of injection current. Furthermore, while the far-fields of the solitary operated BAL exhibit a characteristic flat-top like behavior with lobes at larger diffraction angles, the far-fields emitted by our beam combining setup exhibits a more symmetric lateral shape and relatively enhanced emission around zero divergence angle due to the reinjection of a laterally swapped image from the EC.

Next, we have studied the dependence of the beam combining efficiency on different parameters of the EC. For this reason, we have simulated the coupled BAL+EC system using $I = 12$ A bias current of the individual BALs. The results of this study are summarized in Fig. 6. In the beginning, we have investigated the impact of the focal length of the SAC lenses. As it can be seen from Fig. 6(a), the
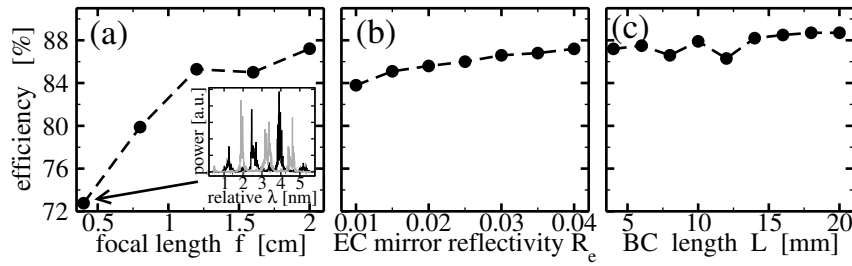
Figure 6: The efficiency of the beam combining as functions of the focal length of SAC lenses f for $L = 4\,\text{mm}$, $R_e = 0.04$ (a), the EC mirror reflectivity R_e for $L = 4\,\text{mm}$, $f = 2\,\text{cm}$ (b), and the BC length L for $R_e = 0.04$, $f = 2\,\text{cm}$ (c). The inset in (a) shows optical spectra of BAL_1 (black) and BAL_2 (grey) for $f = 4\,\text{mm}$.

decrease of f from $20\,\text{mm}$ down to $4\,\text{mm}$ has implied a significant drop of the coupling efficiency. One of the reasons causing the reduction of efficiency, in this case, is an increased filtering spectral band dependence on the lateral position x at the front facet of BALs. Namely, according to (7), the central filtering wavelengths λ_s and λ_c are depending on x:

$$\lambda_c(x) \approx \tilde{\lambda}_0 + j\Delta_\lambda + \frac{L\Delta_{\bar{n}} x^2}{2\bar{n}_1 \bar{n}_2 \lambda_0 f^2}\Delta_\lambda, \ \ \lambda_s(x) \approx \lambda_c(x) + \frac{\Delta_\lambda}{2}, \ \ j \in \mathbb{Z},$$

where $\tilde{\lambda}_0$ is a fixed wavelength in the close vicinity of λ_0. The detuning between λ_s (or λ_c) at $x = \pm\frac{w}{2}$ (edges of the contact bar at the facet) and $x = 0$ (middle of this contact) is $\frac{L\Delta_{\bar{n}} w^2}{8\bar{n}_1 \bar{n}_2 \lambda_0 f^2}\Delta_\lambda$ which, in the considered example, is 2.16% of the wavelength spacing Δ_λ for $f = 4\,\text{mm}$ and less than 0.1% of this spacing for $f = 20\,\text{mm}$. This ratio increases linearly with the increase of BC length L and quadratically with an increase of the contact width w or decrease of the focal length f. An increase of this detuning degrades the filtering of the cavity modes and introduces an additional overlap of the wavelength filters for both coupled BALs. As a consequence, the separation of the spectral combs and, especially, the selection of the cavity modes close to the (unique) positions of λ_s and λ_c is slightly degraded, see, e.g., broadened and strongly scattered spectral comb lines in the inset of Fig. 6(a) and compare them with a better confined spectral comb lines in Fig. 4(a) calculated for $f = 20\,\text{mm}$.

Fig. 6(b) represents our study of the BAL+EC system for different EC mirror reflectivities R_e. On the one hand, the nonvanishing reflection at the mirror is needed to provide the wavelength-filtered feedback which implies an enhancement/suppression of corresponding cavity modes within the BALs. On the other hand, the enhanced reflection would mean the reduced intensity of the combined beam transmitted through the mirror and, additionally, an increased probability of the feedback-induced damages of the front facet coating [12]. For the considered reflectivity range, $R_e \in [1, 4]\%$, we could observe a slight monotonous increase of the coupling efficiency from 84% to 88%. For these R_e, the slight decay of the mirror transmission is compensated by a better feedback-induced filtering of the cavity modes within BALs.

Finally, Fig. 6(c) illustrates the performance of the coupled BALs once exploiting the BCs of different length, $L \in [4, 20]\,\text{mm}$. The remaining major parameters of the EC were fixed at already optimized values of $f = 20\,\text{mm}$ and $R_e = 0.04$. As one can see, the efficiency factor deviates between 86% and 89%, with slightly better values achieved for the longer BCs. This efficiency improvement is consistent with the optical spectra shown in the left panels of Fig. 4. Here, an increase of L leads not only to decrease of the wavelength spacing Δ_λ and of the corresponding Lyot-filter transmission windows but also to a smaller scattering of the separate optical comb lines which is a signature of a more regular enhancement of the cavity modes located close to the optimal λ_s and λ_c.

5 Experiments

The above-discussed polarization and spectral beam combining was tested using different BALs, BAL arrays, as well as slightly different modifications and extensions of the basic setup of Fig. 1. The measurements of all these configurations, in general, have confirmed the possibility to exploit the polarization and spectral beam combining. Namely, measurements of the total combined optical beam and the separate BAL emissions have shown similar near- and far field profiles, and similar widths of the optical spectra. The efficiency η of the beam combining in the considered cases was in the range of $[70, 75]\%$ and still is a subject for further optimization.
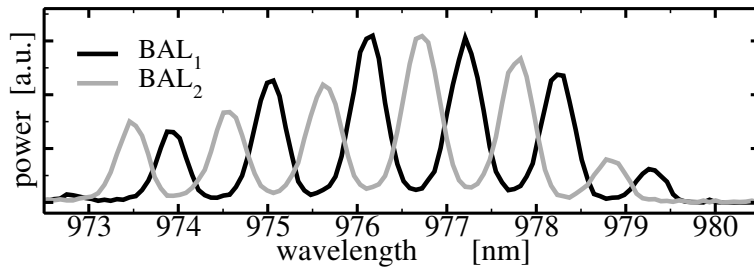

Figure 7: Optical spectra of the emission from separately activated BAL_1 and BAL_2 after the external mirror.

The solid curves in Fig. 7 represent our early measurements of the configuration of Fig. 1. The basic parameters of BALs, in this case, were $l = 4\,\mathrm{mm}$, $w = 100\,\mu\mathrm{m}$, and $R_0 \approx 0.02$. The optical elements of the EC are characterized by $L = 4\,\mathrm{mm}$, $R_e = 0.04$, and $f = 30\,\mathrm{mm}$, whereas the focal length of the fast axis collimator was $2.5\,\mathrm{mm}$. Both BALs were driven with $10\,\mathrm{A}$ bias current, and the intensity of their emission was 4.7 and $4.3\,\mathrm{W}$, respectively.

The inspection of the solid curves in Fig. 7 shows that Lyot-filtered optical feedback allows achieving theoretically demonstrated enhancement of the BAL modes within periodically reappearing wavelength bands, suppression of the BAL modes in the adjacent bands, and alternation of the enhanced spectral components for BAL_1 and BAL_2. The combined field spectrum is of a similar width as those of the separate emitters. The nonvanishing spectral contributions of the individual emitters within the suppressed wavelength bands, however, show an incomplete suppression of the corresponding BAL modes. The nonvanishing contribution of these modes indirectly indicates the presence of the significant y-polarized field component after the forward beam propagation through the BC at these wavelengths and the loss of this component at the PBS_2. As a consequence, the combination of two beams, in this case, has a moderate efficiency factor of $\eta = 57\%$.
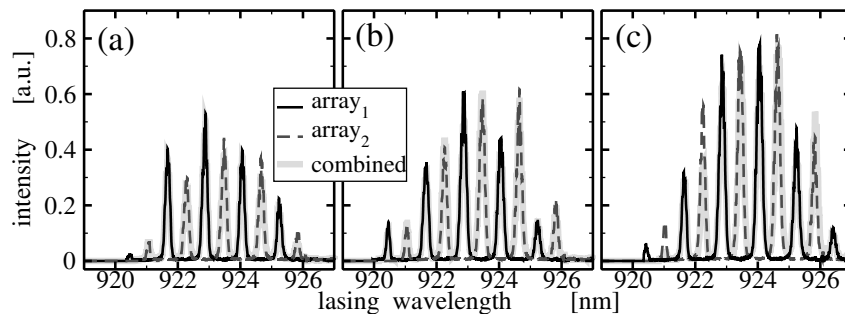

Figure 8: Optical spectra of the separately activated BAL arrays (thin black solid and dashed) and the combined beam (thick grey) for $100\,\mathrm{A}$ (a), $150\,\mathrm{A}$ (b), and $200\,\mathrm{A}$ (c) bias currents applied to each laser bar during $200\,\mu\mathrm{s}$ long intervals at $50\,\mathrm{Hz}$ repetition rate. Each array consists of 23 $4\,\mathrm{mm}$-long emitters having $200\,\mu\mathrm{m}$ wide contacts and $400\,\mu\mathrm{m}$ pitch width.

In the next experimental example, we analyze the polarisation-coupled radiation from two *laser arrays*, each having 23 emitters with $l = 4\,$mm, $w = 200\,\mu$m, $R_0 = 0.04$, and a 50% fill factor. The threshold current of such a laser array is about $24\,$A. The main parameters of the EC are $L = 4\,$mm, $f = 20\,$mm, and $R_e = 0.04$. Instead of simple FAC lenses, we use beam transformation systems (manufactured by LIMO) consisting of a FAC lens with the $356\,\mu$m focal length and an array of biconvex cylindrical lenses positioned at $45°$ to the fast axis and providing a $90°$ twist of each individual BAL emission. As a result, instead of the nicely collimated along the fast (vertical) axis and $\sim 1\,cm$ broad along the slow (horizontal) axis beam of the whole laser array, we get a much more compact beam represented by 23 parallel vertical stripes, each showing lasing of an individual emitter [13]. Once the construction of the EC is perfect, the individual BALs have no cross-feedback from the neighboring emitters of the same array.

The polarization-combining of the beams emitted by two laser arrays is represented in Fig. 8. Here, the laser arrays were biased with the pulsed pump current at $50\,$Hz frequency with $200\,\mu$s-long 100, 150, and $200\,$A bias pulses (duty cycle of 0.01). The mean intensity of the solitary individual arrays and the combined beam behind the EC in these cases were $(81.6, 81.8, 131.1)$ W for the case (a), $(136.1, 137.7, 209.6)$ W for (b), and $(184.5, 185, 276.7)$ W for (c), respectively. The corresponding coupling efficiency for these three cases was 80.2%, 76.6%, and 74.9%. Solid and dashed black curves in these diagrams represent the combined optical spectra of each laser array. In contrast to the situation of Fig. 7, the suppression of the cavity modes within the filtered-feedback-unsupported wavelength bands is nearly perfect, what allows expecting reduction of the field losses at the PBS$_2$. On the other hand, the introduction and possible slight misalignment of beam twisters could cause additional optical losses and the reduction of η.

6 Discussion

The optimal coupling efficiency factor at high intensities in our measurements presented above was not exceeding $\eta = 75\%$, which is significantly less than the optimal factor of $\eta \approx 88\%$ achieved in our simulations. Here we note, that the only reason causing the reduction of η in our model is damping of the residual y-polarized field components (occurring due to insufficient suppression of the corresponding BAL modes by the frequency-filtered optical feedback) at the PBS$_2$. However, the real systems can have other efficiency-limiting reasons, not accounted for in our model so far. Some of them are the nonvanishing field losses within the PBSs or BCs; the losses induced by the non-perfect AR coating, beam collimation within lenses, the polarization switching within the HWP or splitting within the PBS, or by an improper allocation (rotation) of all optical components w.r.t. the optical axes of BALs. Moreover, in the case of laser arrays, we had $5 - 10\%$ depolarization per laser bar which implies the corresponding losses of the emitted fields at the PBS$_1$.

On the other hand, the results presented above have shown that our model and the software tool can recover the experimentally observable dynamics of the pair of lasers or laser bars coupled by the single polarization beam-combining external cavity. Both theoretical and experimental studies have demonstrated that the optical feedback filtered by the Lyot filters can act as an efficient wavelength selection mechanism and that the optical spectra, near- and far- fields of the combined beam remain similar to that one of the solitary laser. Moreover, our efficient modeling of the field propagation in the external cavity of the basic setup of Fig. 1 can be extended to more complex cavities containing additional lenses, BCs, PBSs, and HWPs. In the external cavities where the telescope-like field propagation is no more valid, we still can consequently exploit different beam propagators estimating them when needed with the help of numerically-efficient FFTs. Below we briefly discuss several of such
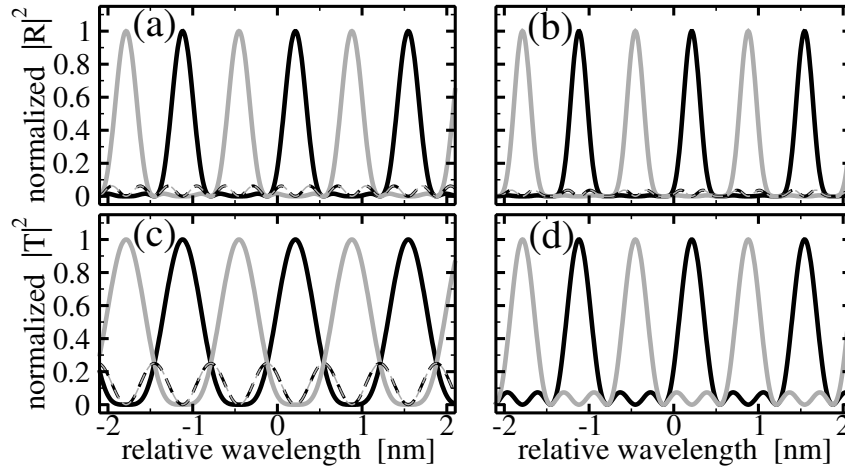
possible extensions of our setup.

Figure 9: Normalized reflection (a,b) and transmission (c,d) spectra of the EC determined in Fig. 1 with an additional BC of the same length (a,c) or a twice longer BC and a PBS (b,d) just before the outcoupling mirror. Black and grey curves represent filtering of the fields emitted by BAL_1 and BAL_2, respectively. Thick solid: self-feedback (a,b) and corresponding main transmission components (c,d). Thin dashed: cross-feedback (a,b) and the transmission of the BAL_1 (BAL_2) emission at the complimentary y- (x-) polarized component, respectively (c). Parameters the same as in Fig. 3.

The improvement of the coupling efficiency can also be achieved by adding another L-long BC or a $2L$-long BC and PBS between the PBS_2 and the external mirror. In the frequency domain, the new component(s) imply additional filtering factors $\cos \gamma'$ or $\cos^2 \gamma'$ for the complex amplitudes of the reinjected fields. When comparing the reflection spectra of both these new configurations, Figs. 9(a) and (b), with the similar spectra of the original setup, Fig. 3(a), one can clearly see that the filtering bands are narrower whereas the contribution of the cross-feedback is decreased. Both these features allow expecting a smaller overlap of the spectra of both lasers and, consequently, better efficiency of the coupled laser system. It is noteworthy that in the case of the first (simpler) extension of the EC the total field $\mathbf{E}$ at the external mirror has both nonvanishing x- and y- polarized components E_x and E_y. The main contribution to the E_x and E_y components is provided by the BAL_1 and BAL_2 (solid black and grey curves in Fig. 9(c)), respectively. The nonvanishing black- and grey- thin dashed curves show also that a smaller portion of the emission from both BALs can reach the external mirror in complimentary polarization state.

One can also extend the BAL+EC setup proposed in Fig. 1 by another pair of lasers, $BAL_{1'}$ and $BAL_{2'}$, which, like in along of our paper discussed configuration, are supplemented by two SAC lenses, the HWP just after the SAC of $BAL_{2'}$, the beam splitter $PBS_{1'}$, and the birefringent crystal $BC_{1'}$. The latter is connected to the free port of the PBS_2 of the original configuration as it is shown in Fig. 1. The configuration of this new two-BAL+EC branch is equivalent to that one considered before, just the combined beam of these new BALs reaching the external mirror has a vanishing x- and a nonvanishing y-polarized component and, therefore, is not interacting with the fields of initially considered configuration at all. One can expect a doubled total emission intensity with the same beam coupling efficiency in this case.

The ideas presented above can be used for further coupling of even more BALs into a single beam-combining scheme. Fig. 9(b) has demonstrated that additional BC and PBS can be helpfull in achieving a better frequency filtering and, consequently, a better mode selection in BALs. On the other hand, a free port of the newly introduced PBS can be used for a coupling of another set of lasers. A further

Appendix

The field propagation in a homogeneous material with refractive and group indices $\bar{n}$ and $\tilde{n}$ between two to the optical axis perpendicular planes separated by a distance d is defined by the propagation operator $M_d^{\mathrm{pr}}[\bar{n}, \tilde{n}]$:

$$
\begin{aligned}
E(z' + d, x, t) &= M_d^{\mathrm{pr}}[\bar{n}, \tilde{n}] E(z', x, t) \\
&= \sqrt{\frac{i\bar{n}}{\lambda_0 d}} \, e^{-i\bar{n}k_0 d} \int_{\mathbb{R}} e^{-i\frac{\bar{n}k_0}{2d}(x'-x)^2} M_{d\tilde{n}/c_0}^{\mathrm{sh}} E(z', x', t) dx',
\end{aligned}
$$

where $\frac{d\tilde{n}}{c_0}$ is a propagation time through the material. Note, that

$$
M_d^{\mathrm{pr}}[\bar{n}, \tilde{n}] = e^{-id\frac{(\bar{n}^2-1)k_0}{\bar{n}}} M_{d/\bar{n}}^{\mathrm{pr}} M_{\frac{d}{c_0}(\tilde{n}-\frac{1}{\bar{n}})}^{\mathrm{sh}}, \quad M_{d'}^{\mathrm{pr}} = M_{d'}^{\mathrm{pr}}[1, 1].
$$

The field transmission through the thin slow-axis collimating lens with a focal length f located perpendicularly to the optical axis at $z = z'$ is given by

$$
E(z'_+, x, t) = M_f^{\mathrm{ln}} E(z'_-, x, t), \quad M_f^{\mathrm{ln}}(x) = e^{i\phi_{\mathrm{ln}}} e^{i\frac{k_0}{2f}x^2},
$$

where ϕ_{ln} is a phase factor determined by the refractive index and thickness of the lens, z_- and z_+ are two sides of the lens. Note also that the free-space propagator between the outer focal planes of two perpendicularly to an optical axis located lenses (telescope configuration) can be written as:

$$
\begin{aligned}
M_{f,\delta}^{\mathrm{tel}} &= M_f^{\mathrm{pr}} M_f^{\mathrm{ln}} M_{2f+\delta}^{\mathrm{pr}} M_f^{\mathrm{ln}} M_f^{\mathrm{pr}} \\
&= e^{i(2\phi_{\mathrm{ln}}-(4f+\delta)k_0)} e^{i\frac{\delta k_0}{2f^2}x^2} M^{\mathrm{sw}} M_{(4f+\delta)/c_0}^{\mathrm{sh}}.
\end{aligned}
$$

The interaction of horizontally and vertically polarized components E_x and E_y of the vector-field $\mathbf{E}$ within the BC of length L is given by

$$
\begin{aligned}
\mathbf{E}(z' + L, x, t) &= \mathbf{M}_L^{\mathrm{bc}} \mathbf{E}(z', x, t), \quad \text{where} \\
\mathbf{M}_L^{\mathrm{bc}} &= \sigma^+ M_L^{\mathrm{pr}}[\bar{n}_1, \tilde{n}_1] + \sigma^- M_L^{\mathrm{pr}}[\bar{n}_2, \tilde{n}_2], \\
\sigma^{\pm} &= \frac{\sigma^d \pm i\sigma^a}{2}, \quad \sigma^d = \begin{pmatrix} 1 & 0 \\ 0 & 1 \end{pmatrix}, \quad \sigma^a = \begin{pmatrix} 0 & -i \\ -i & 0 \end{pmatrix}.
\end{aligned}
$$

Propagation through the HWP is governed by the same operator applied to the BC of length $\lambda_0/(2(\bar{n}_1 - \bar{n}_2))$. By neglecting small, short-range angular dispersion and time delays induced by the HWP, we effectively reduce this operator:

$$
\mathbf{M}^{\mathrm{wp}} = \mathbf{M}_{\lambda_0/(2(\bar{n}_1-\bar{n}_2))}^{\mathrm{bc}} \approx e^{i\phi_{\mathrm{wp}}} \sigma^a, \quad \phi_{\mathrm{wp}} = -\frac{\pi}{2}\frac{\bar{n}_2+\bar{n}_1}{\bar{n}_1-\bar{n}_2}.
$$

The transmission of the ideal PBS along and perpendicularly to the incident beam are given by simple projectors,

$$
\mathbf{M}_1^{\mathrm{bs}} = \sigma^x = \begin{pmatrix} 1 & 0 \\ 0 & 0 \end{pmatrix}, \quad \mathbf{M}_2^{\mathrm{bs}} = \sigma^y = \begin{pmatrix} 0 & 0 \\ 0 & 1 \end{pmatrix}.
$$

The ignored physical length of the HWPs and PBSs in our model can be compensated by the artificially increased widths of the nearby located air gaps.

Next, we note several properties of the above-defined operators. Two consequently applied operators M^{pr} can be combined into the single one, $M^{\mathrm{pr}}_{d'} M^{\mathrm{pr}}_{d''} = M^{\mathrm{pr}}_{d'+d''}$. The same property is valid for M^{sh}. Scalar operators M^{pr} and M^{ln} are commuting with any of simple matrix operators $\mathbf{M}^{\mathrm{bs}}_1$, $\mathbf{M}^{\mathrm{bs}}_2$, $\mathbf{M}^{\mathrm{wp}}$, whereas M^{pr} is additionally commuting with a BC operator $\mathbf{M}^{\mathrm{bc}}_L$. M^{sw} and M^{sh} commute with all above discussed operators. All these properties allow exchanging the corresponding optical elements and the air gaps (see Fig. 1) in our modeling, "concentrating" all the air gaps into the gaps of width f between the front facet of BAL$_j$ and the corresponding lens (the HWP, if present, is "shifted" directly to the front facet of the BAL) and of width l_j between the lens of BAL$_j$ and PBS$_1$. Now the frequency-filtering propagator of the vector-field $\mathbf{E}$ in common for both considered BALs part of the EC (the BC, PBS$_2$ and the external mirror) can be written as

$$\mathbf{M}^{\mathrm{fl}} = \sqrt{R_e}\, \mathbf{M}^{\mathrm{bc}}_L \mathbf{M}^{\mathrm{pbs}}_1 \mathbf{M}^{\mathrm{bc}}_L = \frac{\sqrt{R_e}}{4} \sum_{l=1}^{3} \xi_l \sigma_l M^{\mathrm{pr}}_{d_l} M^{\mathrm{sh}}_{\tau_l},$$
$$\text{where} \quad \sigma_1 = 2\sigma^+, \quad \sigma_2 = 2\sigma^-, \quad \sigma_3 = \sigma^x - \sigma^y,$$

whereas ξ_l, d_l, τ_l for $l = 1, 2, 3$ are defined in (8). The vector-field propagator from BAL$_j$ to BAL$_r$ is given by

$$\mathbf{M}_{[r,j]} = \mathbf{M}'^{T}_{[r]} \mathbf{M}^{\mathrm{fl}} \mathbf{M}'_{[j]}, \quad \mathbf{M}'_{[j]} = \mathbf{M}^{\mathrm{bs}}_j M^{\mathrm{pr}}_{l_j} M^{\mathrm{ln}}_f M^{\mathrm{pr}}_f \mathbf{M}^{\mathrm{wp}}_j,$$

where $\mathbf{M}'_{[j]}$ and the transposed matrix-operator $\mathbf{M}'^{T}_{[j]}$ propagate the vector-field from the BAL$_j$ to the BC and back, whereas $\mathbf{M}^{\mathrm{wp}}_j = \mathbf{M}^{\mathrm{wp}}$ for $j = 2$ (the HWP is present) and is an identity operator σ^d otherwise. Like the filtering operator $\mathbf{M}^{\mathrm{fl}}$, the propagator $\mathbf{M}_{[r,j]}$ can also be defined as a sum of three operators, where each (l-th) summand is defined by scalar multipliers, superposition of several scalar operators, and simple matrices. Due to commuting of corresponding operators, the scalar operators can be "shifted" to one side of each of these composite propagators and interpreted as a telescope operator M^{tel} and the time shift:

$$\mathbf{M}_{[r,j]} = \frac{\sqrt{R_e}}{4} \sum_{l=1}^{3} (M^{\mathrm{tel}}_{f,\delta^l_{r,j}} M^{\mathrm{sh}}_{\tau_l}) \Big(\xi_l \mathbf{M}^{\mathrm{wp}}_r \mathbf{M}^{\mathrm{bs}}_r \sigma_l \mathbf{M}^{\mathrm{bs}}_j \mathbf{M}^{\mathrm{wp}}_j \Big).$$

The product of the matrix operators in the considered EC is proportional to the projector σ^x for all combinations of r, j, and l, i.e., $\mathbf{M}_{[r,j]} = M_{[r,j]} \sigma^x$. The definition of scalar feedback operators $M_{[r,j]}$ is given in (6), whereas the parameters used there are

$$\begin{aligned}
\delta^l_{r,j} &= l_j + d_l + l_r - 2f, \quad \tau^l_{r,j} = \tau_l + \frac{4f + \delta^l_{r,j}}{c_0}, \\
\xi^l_{r,j} &= \xi_l (-i e^{i\phi_{\mathrm{wp}}})^{j+r-2} [\sigma_l]_{r,j}\, e^{i(2\phi_{\mathrm{ln}} - (4f + \delta^l_{r,j})k_0)}, \\
d_l &= \frac{2L}{\bar{n}_l}, \ \tau_l = \frac{d_l(\tilde{n}_l \bar{n}_l - 1)}{c_0}, \ \xi_l = e^{i d_l k_0(1 - \bar{n}_l^2)}, \ l = 1, 2, \\
d_3 &= \frac{d_1 + d_2}{2}, \quad \tau_3 = \frac{\tau_1 + \tau_2}{2}, \quad \xi_3 = 2e^{i d_3 k_0(1 - \bar{n}_1 \bar{n}_2)}.
\end{aligned} \tag{8}$$

When considering frequency (wavelength) domain representation (7) of the same operators $M_{[r,j]}$, we use the parameters

$$\begin{aligned}
\xi' &= e^{i\big[2\phi_{\mathrm{ln}} - Lk_0\big((\bar{n}_1 + \bar{n}_2)\big)\big(1 - \frac{x^2}{2\bar{n}_1 \bar{n}_2 f^2}\big) + \frac{\omega'(\tilde{n}_1 + \tilde{n}_2)}{c_0 k_0}\big]}, \\
\hat{\xi}_{r,j} &= e^{i\big[(r+j-2)\phi_{\mathrm{wp}} - (l_j + l_r + 2f)(k_0 + \frac{\omega'}{c_0}) + (l_j + l_r - 2f)\frac{k_0 x^2}{2f^2}\big]}.
\end{aligned} \tag{9}$$

Acknowledgments

References

[1] P. Crump, H. Wenzel, G. Erbert, and G. Tränkle, "Progress in increasing the maximum achievable output power of broad area diode lasers," *SPIE Proc. Series* **8241**, 82410U, 2012.

[2] T.Y. Fan, "Laser beam combining for high-power, high-radiance sources," *IEEE J. Sel. Top. Quantum Electron.* **11**(3), pp. 567–577, 2005.

[3] V. Raab and C. Raab, "Mehrstufige Polarisationskopplung," *Zeitschrift Photonik*, **5**(5), pp. 46–49, 2004.

[4] M. Radziunas, "Modeling and simulations of broad-area edge-emitting semiconductor devices," *The Int. J. of High Perform. Comp. Appl.*, **32**(4), pp. 512–522, 2018.

[5] M. Radziunas et al., "Modeling and simulation of high-power broad-area semiconductor lasers with optical feedback from different external cavities," *Proc. of 26th IEEE International Semiconductor Laser Conference (ISLC 2018)*, Santa Fe, New Mexico, USA, September 16-19, pp. 7–8, 2018.

[6] A. Zeghuzi et al., "Influence of nonlinear effects on the characteristics of pulsed high-power broad-area distributed Bragg reflector lasers," *Opt. and Quantum Electron.*, **50**, 88, 2018.

[7] A.I. Bawamia et al., "Experimental determination of the thermal lens parameters in a broad area semiconductor laser amplifier," *Applied Physics B*, **97**(1), pp. 95–101, 2009.

[8] S. Rauch et al., "Impact of longitudinal refractive index change on the near-field width of high-power broad-area diode lasers," *Appl. Phys. Lett.* **110**(26), 263504, 2017.

[9] "BALaser: a software tool for simulation of dynamics in Broad Area semiconductor Lasers," `http://www.wias-berlin.de/software/BALaser`.

[10] M. Radziunas and R. Čiegis, "Effective numerical algorithm for simulations of beam stabilization in broad area semiconductor lasers and amplifiers," *Math. Model. and Anal.*, **19**, pp. 627–644, 2014.

[11] J. J. Gil, E. Bernabeu, "Obtainment of the polarizing and retardation parameters of a non-depolarizing optical system from the polar decomposition of its Mueller matrix," *Optik* **76**, pp. 67–71, 1987.

[12] S. Rauch, C. Holly, and H. Zimer, "Catastrophic Optical Damage in 950-nm Broad-Area Laser Diodes Due to Misaligned Optical Feedback and Injection," *IEEE J. of Quantum Electron.* **54**(4), 2000707, 2018.

[13] Junhong Yu et al., "Optimization of beam transformation system for laser-diode bars," *Opt. Express* **24**, pp. 19728–19735, 2016.